Estimation of high-resolution solar irradiance data using optimized semi-empirical satellite method and GOES-16 imagery

Shanlin Chen [a], Zhaojian Liang [a], Su Guo [b,c], Mengying Li [a,d,*]

[a] *Department of Mechanical Engineering, The Hong Kong Polytechnic University, Hong Kong Special Administrative Region*
[b] *College of Energy and Electrical Engineering, Hohai University, Nanjing, China*
[c] *Nanjing Jurun Information Technology Co., Ltd, Nanjing, China*
[d] *Research Institute for Smart Energy, The Hong Kong Polytechnic University, Hong Kong Special Administrative Region*

ARTICLE INFO

ABSTRACT

Semi-empirical satellite method is widely used in estimating global horizontal irradiance (GHI), where various clear-sky models, cloud index (CI) and clear-sky index (CSI) derivation methods are available. This study aims to optimize the semi-empirical satellite model for 5-minute GHI estimation from four aspects: satellite-bands, CI and CSI derivation methods, and clear-sky models. The results show that it achieves better GHI estimates using the blue band, CI derived from monthly fixed upper and lower bounds, and a piecewise CI-to-CSI function. There is no significant difference in all-sky GHI estimation for the clear-sky models regarding normalized root mean squared error (nRMSE, 25.19%–25.53%), which is comparable with the referenced physical model. Clouds cause the largest uncertainty, where the nRMSE is in the range of 37.60%–38.36% in cloudy days and 31.12%–31.54% in cloudy periods. In the application of semi-empirical method with different clear-sky models, Ineichen–Perez has the highest bias of -4.62% in clear days and -3.93% in cloudless periods. REST2 outperforms McClear with slightly lower nRMSE and normalized mean bias error (nMBE) under all sky conditions. McClear is recommended due to its global availability. Modified Ineichen–Perez produces the lowest nRMSE and nMBE using clear-sky GHI as the GHI estimates for clear periods, therefore has the potential for improvements in physical methods.

1. Introduction

Solar radiation is a significant source of renewable energy systems, which can be directly captured to produce heat and electricity. It is reported that solar thermal technologies produced 479 TWh energy in 2019, which is an equivalent energy savings of 43 million tons of oil and 130 million tons emissions of CO_2 (Murphy, 2021). Meanwhile, solar photovoltaic (PV) has also been one of the most promising renewable energy technologies in recent years with an estimated average yearly growth of 15% between 2019 and 2030 (IEA, 2020). However, the power output of a solar energy system is highly variable due to the intermittent and uncertainty of local irradiance conditions (Inman et al., 2013; Chu et al., 2016; Li et al., 2016; Chu et al., 2021). The variability in power production also introduces difficulties in system operation (Chu et al., 2013). Considering the rapid expansion of solar energy conversion applications, it is important to have reliable and accurate ground solar irradiance data at the location of interest. Historical data is essential for the feasibility and optimal system design phases of a solar power conversion project to support decision making and reduce the risk (Kleissl, 2013).

Ground-based measurement is the most reliable irradiance data source for solar energy applications. However, due to difficulties in routine calibration, data quality control, as well as the high cost associated with the instrumentation, complete and long-term ground-based measurements are scarce (Yagli et al., 2020). Therefore, solar irradiance estimation and reanalysis from satellite offer an alternative to the ground measurements for evaluating and designing the solar energy projects (Ayompe and Duffy, 2014). Despite the general belief that solar irradiance data based on satellite observation and model reanalysis is less accurate than ground-based measurements, satellite-derived solar irradiance data can help with model development (Yagli et al., 2020).

As an essential part for solar irradiance modeling, geostationary satellites are widely used for resource monitoring and assessment as they observe continuously the same part of the Earth (Kleissl, 2013). The advancement in modern remote sensing technique brings data in finer temporal and spatial resolutions as well as new insights in solar irradiance modeling. Satellite-based solar irradiance models can be broadly classified as physical, empirical, and semi-empirical methods (Kleissl, 2013). Physical methods usually apply radiative transfer

---

models (RTMs) through different layers in the atmosphere, which requires detailed and accurate information of the atmospheric constituents, such as cloud optical properties, aerosol optical depth (AOD), and water vapor content (Kleissl, 2013). Pure empirical models attempt to simulate the regression between the satellite measurements and ground based records (Kleissl, 2013). While semi-empirical models are a combination of physical and empirical method, which apply a simple RTM and regression approach to fit the observations (Kleissl, 2013).

Many studies have been conducted to estimate the global horizontal irradiance (GHI) from geostationary satellites images (Sengupta et al., 2018; Qu et al., 2017; Hammer et al., 2003; Garniwa et al., 2021). Both physical and semi-empirical models are extensively used in estimating GHI while simple empirical methods are barely applied due to their inferior performance caused by the lack of generality (Garniwa et al., 2021; Laguarda et al., 2020). Physical models usually have better performance than semi-empirical methods (Garniwa et al., 2021), as they technically need the details of atmospheric compositions. For instance, the national solar radiation database (NSRDB) (Sengupta et al., 2018), as a widely accessed and publicly available data source, provides broadband irradiance and other auxiliary variables. NSRDB is produced using the physical solar model (PSM) and products from a number of associations (Sengupta et al., 2018). The Heliosat−4 method (Qu et al., 2017) is also a fully physical model using a fast, approximated, but still accurate RTM approach. Heliosat−4 consists of two models based on libRadtran (Mayer and Kylling, 2005) and look-up tables: the McClear (Lefèvre et al., 2013) for solar irradiance under cloud free conditions and the McCloud for irradiance attenuation due to clouds. However, apart from the complexity and high computing resource requirement, the essential inputs of physical models, such as water vapor, AOD, and cloud properties are difficult to obtain and generally associated with uncertainties (Kleissl, 2013; Zhong and Kleissl, 2015; Larson et al., 2020).

On the other hand, semi-empirical methods typically deal with the irradiance attenuation of atmospheric constituents and cloud extinction separately, with a clear-sky model for clear-sky irradiance and a cloud index (CI) derived from satellite image to account for cloud attenuation (Kleissl, 2013; Hammer et al., 2003). Heliosat method series (Beyer et al., 1996; Rigollier et al., 2004; Mueller et al., 2004) are examples of semi-empirical models, which offer easy implementation, fast calculation and operation (Garniwa et al., 2021). Many clear-sky models have been used in semi-empirical models for GHI estimation, such as the Ineichen–Perez model (Ineichen and Perez, 2002) in the operational model (SUNY model) developed by Perez et al. (2002), the McClear model in the work of Jia et al. (2021), and the REST2 (Gueymard, 2008) model in Solcast (Solcast, 2021). There are also different methods proposed to calculate the GHI based on clear-sky index (CSI) and CI in the literature (Hammer et al., 2003; Perez et al., 2002; Mueller et al., 2012).

Given that a variety of clear-sky models are available for estimating GHI in semi-empirical satellite models with different regressions between CSI and CI, there has been a dearth of study to compare the performance of different clear-sky models and empirical relationships for GHI estimation. Some related studies from the literature are summarized as follows, Rigollier and Wald (1999b) compared several clear-sky models developed at the early stages and selected the ESRA (Rigollier et al., 2000) model for the HelioClim project (Rigollier and Wald, 1999a), which was later replaced by McClear for improvements (Qu et al., 2014). Laguarda et al. (2020) applied the ESRA and McClear model in hourly GHI estimation over the Pampa Húmeda with different locally adjusted CI methods. McClear model performs better than ESRA model under clear-sky conditions, and both ESRA and McClear models have small negative biases of −1.1% for all-sky GHI estimates while McClear yields a slightly lower relative root mean square deviation (rRMSD, 12.5% versus 12.1%). Garniwa et al. (2021) analyzed the performance of different semi-empirical models for hourly GHI estimation in Korea and found the Hammer model presented in Hammer

et al. (2003) has a better result. Meanwhile, a hybrid model was also proposed with smaller root mean square error (RMSE) than the Hammer model (97.08 W m^{-2} versus 103.92 W m^{-2}). However, limited studies have been conducted to compare and evaluate the performance of different clear-sky models, CI and CSI derivation methods in solar resourcing. Considering the advanced clear-sky models have been developed with high performance and much finer resolution of the data (e.g., 5 min images) provided by modern satellites, it would be of interest to compare and evaluate the methods and clear-sky models used in semi-empirical model for GHI estimation with a fine spatiotemporal resolution (i.e., 5 min and 1 km).

This study aims to optimize the semi-empirical satellite model for 5 min GHI estimation via comparing and evaluating the performance of different clear-sky models, CI and CSI derivation methods, and satellite bands. Ineichen–Perez, McClear, and REST2 are compared as the representatives of average, good and best clear-sky models to keep the generality (Yang, 2020). The main contributions of this work are summarized as follows:

- Evaluates the performance of 5 min all-sky GHI estimate based on different bands of GOES-16 and different empirical relationships between CSI and CI.
- Compares different methods to derive the CI based on GOES-16 data for 5 min GHI estimation, in particular, the used time window, determinations of upper and lower bounds.
- Introduces the modified Ineichen–Perez clear-sky model based on estimated turbidity from local meteorological measurements (Chen and Li, 2022) in all-sky GHI estimation.
- Compares and evaluates the four aforementioned clear-sky models for estimating 5 min GHI using semi-empirical methods under different sky conditions.

The remainder of this work is structured as follows: Section 2 describes the used data, semi-empirical GHI estimation method, and the details of the compared clear-sky models. The performance of different CI, CSI calculation methods, and different clear-sky models for GHI estimation and discussions are presented in Section 3. Finally, the key findings of this study and recommendations are summarized in Section 4.

2. Data and methods

This section describes the used data and the semi-empirical satellite method for GHI estimation. The satellite data will first undergo a radiance conversion to eliminate the negative points, then the CI and CSI are determined using different strategies and methods that are described in Section 2.2. Finally, the GHI is calculated via the CSI and clear-sky GHI (GHIcs) from the clear-sky model as shown in Fig. 1. Four clear-sky models are compared, the GHIcs of REST2 and McClear are publicly available, Ineichen–Perez documented in PVLIB (Holmgren et al., 2018) adopts the default calculations, while Ineichen–Perez TL model uses the estimated turbidity based on local meteorological measurements (Chen and Li, 2022). The detailed method for estimating turbidity is presented in Section 2.3.

2.1. Data

The satellite data used in this work is from GOES-16, operated by National Oceanic and Atmospheric Administration (NOAA). GOES-16 has 16 spectral bands, the Advanced Baseline Imager (ABI) provides data with temporal resolution of 5–15 min, and spatial resolution of 0.5–2 km at the sub-satellite point (Schmit et al., 2018). In this study, the data from two visible bands (blue, red) and one near-infrared band (veggie) in the year of 2019 are retrieved from publicly available sources and then georeferenced to the ground location of interest, the detailed information about the aforementioned bands is presented in Table 1. There are three UTC (Universal Time Coordinated) timestamps
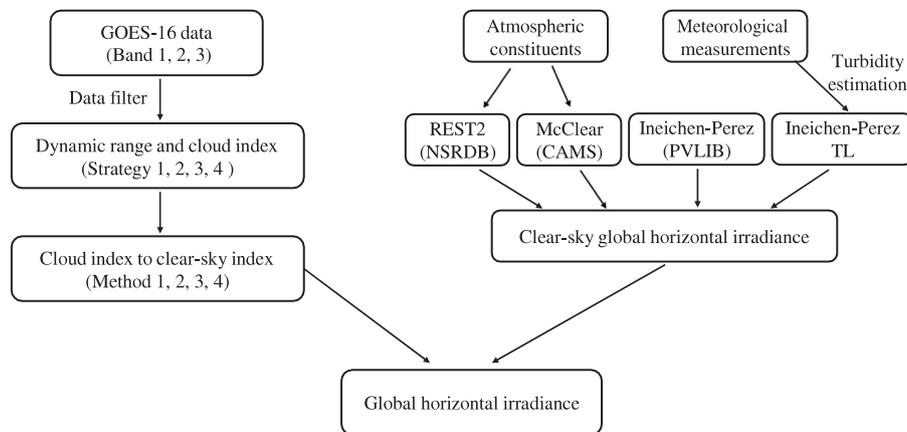
Fig. 1. The flowchart of GHI estimation using semi-empirical methods with different clear-sky models.

Table 1
Summary of the blue, red, veggie bands of GOES-16. All the information is obtained from the GOES-R Series Product Definition and User's Guide (PUG) (goe, 2019).

Band No.	Type	Center wavelength (Range) [μm]	Resolution [km]	Valid range[a]	Scale factor	Add offset
1 (Blue)	Visible	0.47 (0.450–0.490)	1.0	0–1022	0.8121	−25.9366
2 (Red)	Visible	0.64 (0.590–0.690)	0.5	0–4094	0.1586	−20.2899
3 (Veggie)	Near-Infrared	0.87 (0.846–0.885)	1.0	0–1022	0.3769	−12.0376

[a]Valid range is in packed and scaled integer form. Scale factor and add offset are used to convert scaled integer to physical quantity, which is radiance [$W\,m^{-2}\,sr^{-1}\,\mu m^{-1}$] in this case.

Table 2
Summary of the seven SURFRAD stations.

Station	Latitude (°)	Longitude (°)	Altitude (m)	Timezone	Snow-free period
BON	40.05	−88.37	230	UTC-6	2019-04-01–2019-10-31
DRA	36.62	−116.02	1007	UTC-8	2019-01-01–2019-12-31
FPK	48.31	−105.10	634	UTC-7	2019-05-03–2019-09-30
GWN	34.25	−89.87	98	UTC-6	2019-01-01–2019-12-31
PSU	40.72	−77.93	376	UTC-5	2019-04-01–2019-10-31
SXF	43.73	−96.62	473	UTC-6	2019-05-01–2019-09-30
TBL	40.12	−105.24	1689	UTC-7	2019-05-02–2019-09-30

referring the time of file creation, start and end of the scan. To be compatible with ground measurements and real-time applications, the end timestamp is applied to index the data after rounded to the next nearest 5 min interval.

The corresponding ground irradiance measurements are from the stations in Surface Radiation Budget Network (SURFRAD) (Augustine et al., 2000). Detailed information of the seven stations are summarized in Table 2. The initial dataset includes a variety of 1-minute averaged solar irradiance as well as meteorological information. Ambient air temperature, relative humidity, wind speed and atmospheric pressure are averaged on a daily basis (when solar zenith angle is less than 85°) for turbidity estimation, and GHI is averaged on a basis of 5 min. The quality control (QC) for meteorological recordings is available in the original dataset, any data point does not meet the QC is excluded when calculating the daily average. The QC procedure for GHI follows the steps detailed in Yang (2021), any 1-minute data points do not pass the QC are discarded when aggregating the GHI to 5 min resolution in the round way (i.e., data points from 13:58, 13:59, 14:00, 14:01, 14:02 are aggregated and indexed as 14:00).

The 5 min satellite-derived GHI at the SURFRAD stations in the year of 2019, provided by NSRDB (Sengupta et al., 2018), is also used in this work for comparison. NSRDB is produced using the PSM and REST2 (Gueymard, 2008) clear-sky model (the GHIcs estimation from REST2 is also available in NSRDB), the spatiotemporal resolution is improved to 5 min and 2 km.

Without extra algorithm for cloud and snow detection, semi-empirical models (e.g., Heliosat method) could not account for the significant changes in the ground surface albedo due to the snow cover, which may introduce large uncertainty and unreliability in deriving surface solar irradiance (Kallio-Myers et al., 2020). Therefore, the GHI estimation and comparison are performed in the snow-free periods for all the SURFRAD stations. The information of snow depth is available from the dataset of National Aeronautics and Space Administration (NASA) National Snow and Ice Data Center (NSIDC) (Broxton et al., 2019; Zeng et al., 2018). We use data in full months, however, a month having only a few days detected with snow cover at the beginning (or ending) is also included after removing the snow-present days. The detailed information of snow-free periods at all SURFRAD stations could be found in Table 2.

2.2. Semi-empirical models

Semi-empirical models are typically developed to exploit data recorded by the visible channel of a geostationary satellite (Kleissl, 2013), which can be traced from the contribution of Cano et al. (1986). Compared with physical methods, semi-empirical models use a simplified radiative-transfer approach (Kleissl, 2013), which are extensively used in solar resourcing (Albarelo et al., 2015; Lorenzo et al., 2017; Mouhamet et al., 2018) and forecasting (Kallio-Myers et al., 2020; Arbizu-Barrena et al., 2017; Harty et al., 2019) applications.

The underlying idea of semi-empirical method is to estimate the global surface solar irradiance from satellite measurements considering atmospheric and cloud attenuation separately (Hammer et al., 2003). In the first step the clear-sky irradiance is derived for a given location

Table 3
Summary of the strategies used to derive CI for GHI estimation.

Strategy	Time window[a]	Upper bound	Lower bound	Reference
1	90 days (moving)	mean of 20 highest values	mean of 40 lowest values	Perez et al. (2002)
2	60 days (moving)	mean of 20 highest values	mean of 40 lowest values	Harty et al. (2019)
3	30 days (moving)	mean of 10 highest values	mean of second to fifth lowest values	
4	1 month (fixed)	mean of 10 highest values	mean of second to fifth lowest values	

[a]Time window is used to determine the dynamic range, a moving time window means it moves with the time of interest, so the upper and lower bound will change. While the monthly fixed time window means it is fixed in the month of interest, so the upper and lower bounds remain constant in the month.

and time via a clear-sky model. In the second step the cloud attenuation is determined from the visible radiance by introducing CI, which is then correlated to CSI. Finally, the global surface solar irradiance is calculated from the clear-sky irradiance and CSI (Hammer et al., 2003).

The CI for the SURFRAD stations are calculated following the methods presented in Perez et al. (2002). First, the pixel value is normalized:

$$\text{norpix} = \text{pix} \cdot \text{AM} \cdot \text{soldist} \tag{1}$$

where pix is the satellite pixel intensity, AM is the absolute airmass, and soldist [AU] is the Sun–Earth distance. In the original proposed method in Perez et al. (2002), the raw data such as digital number (digital count) is used as the pixel intensity. In this work, we first convert the digital number (scaled integer) to the radiance via the scale factor and add offset as shown in Table 1, and eliminate the negative data points considering the radiance measured by the ABI sensor should not be negative. Note that this step does not show much difference with the original method but discarding some data points, as the raw pixels are proportional to the Earth's radiance observed by the satellite (Perez et al., 2002) and the linear transformation does not introduce any non-linearity.

To account for high airmass effect, the normalized pixels considered for dynamic range maintenance are subjected to a secondary normalization:

$$\text{npix} = \text{norpix}/(2.283h^{-0.26} \cdot \exp(0.004h)) \tag{2}$$

where h [°] is the solar elevation, which is in the range of 1.5° to 65° and the value is set to be 65° when the solar elevation is greater than 65°. Note that although solar elevations of low and medium airmass are included, they have different normalization extents, where the high airmass effects could be accounted for.

Then the CI value is determined by:

$$\text{CI} = \frac{\text{npix} - low}{high - low} \tag{3}$$

where $high$ is equal to the mean of the 10 highest npix values in a month to estimate the upper dynamic range, while low is calculated as the mean of the second to the fifth lowest values for that time of the day in a month, the lowest value is excluded due to its variation and the undetected defects in the original image (Rigollier et al., 2004; Albarelo et al., 2015). Our method for determining the upper and lower bond is different from the methods presented in Ineichen and Perez (2002), Lorenzo et al. (2017) and Harty et al. (2019), the time window is one month to better account for the seasonal variations of the ground reflectance (Hammer et al., 2003; Williamson et al., 2018). Meanwhile, the low is calculated every 5 min for time in the day (when the solar zenith angle is less than 80°) taking advantage of the improved time resolution of GOES-16. Four strategies for CI derivation are compared in this work, where Table 3 details the used time window, the determinations of upper and lower bounds in each strategy.

After the derivation of CI, the next step is the conversion from CI to CSI and then to GHI. Similarly, there are also different methods proposed as shown in Table 4. In general, CI is first converted to CSI via an empirical method, GHI is then calculated based on CSI and GHIcs, where GHIcs [W m^{-2}] is the clear-sky GHI estimated from the

chosen clear-sky model. In the development of the CI-to-CSI methods, Perez et al. (2002) compares the old method (Method 1) and newly-developed method (Method 2) using GOES-8 and GOES-10 satellites, and the involved ground stations are Albany (New York), Burlington (Kansas), Eugene, Gladstone, and Hermiston (Oregon). Method 3 presented in Hammer et al. (2003) and Method 4 proposed in Mueller et al. (2012) are developed using Meteosat series of satellites and ground stations in Europe. Therefore, the use of SURFRAD stations in the comparison of the CI-to-CSI methods is acceptable since they are not involved in the methods development.

In this study, we apply and compare four clear sky models, namely, the Ineichen–Perez model (Perez et al., 2002) documented in PVLIB (Holmgren et al., 2018) using default turbidity interpolated from SoDa monthly climatology mean database (Remund et al., 2003), the McClear model (Lefèvre et al., 2013), the REST2 model (Gueymard, 2008), and the Ineichen–Perez model using turbidity estimated from the local meteorological measurements (Chen and Li, 2022) (hereafter referred as Ineichen–Perez TL model). Table 5 summarizes the input parameters for the aforementioned clear-sky models. The detailed method of estimating the turbidity is introduced in the following subsection. McClear model and REST2 model are physical models, which might be generally superior to those models taking reduced forms or using approximations (Yang, 2020). However, the physical models are of much more complexity due to their prevailing atmospheric conditions on the attenuation constituents and the application of RTMs. For instance, the REST2 model has repeatedly been validated as one of the models with high-performance (Yang, 2020), but it requires at least nine input parameters, and some of them such as AOD at 550 nm, amount of ozone, and precipitable water are difficult to obtain Yang (2020) and Zhong and Kleissl (2015). The clear-sky irradiance of REST2 used in this work is from the database of NSRDB. The McClear is also a fully physical model requiring input parameters regarding the optical property of the atmosphere, e.g., the amount of ozone, precipitable water, and AOD at 550 nm (Lefèvre et al., 2013). McClear applies a lookup table to speed up the calculation of RTMs, and the clear-sky irradiance is available from the Copernicus Atmosphere Monitoring Service (CAMS) (Schroedter-Homscheidt et al., 2021). The time resolution is from 1 min to 1 month in the time range of 2004-01-01 up to two days ago.

2.3. Turbidity estimation

The original method of estimating turbidity via local meteorological measurements is presented in Chen and Li (2022). Although the original model is trained based on the data samples focused on clear-sky days, the results show that the method can also be applied to estimate the turbidity in partially clear days. In this work, the data samples from partially clear days are also included in the model training following the same methodology described in Chen and Li (2022). In specific, the data used in turbidity estimation for SURFRAD stations are in the year range of 2010 to 2018. The clear-sky instants are detected by the Bright-Sun method described in Bright et al. (2020), and the solar zenith angle is set to be less than 85° as the turbidity exhibits high variations during sunrise and sunset (Chen and Li, 2022). To better represent the GHIcs-derived turbidity on a daily basis, only a day with

Table 4

Different methods to calculate GHI via CSI, CI and GHIcs. GHIcs is estimated from a selected clear-sky model.

Method	GHI calculation	Reference
1	GHI = GHIcs · CSI CSI = 0.02 + 0.98 · (1 − CI)	Perez et al. (2002)
2	GHI = CSI · GHIcs · (0.0001 · CSI + 0.9) CSI = $2.36 \cdot CI^5 - 6.3 \cdot CI^4 + 6.22 \cdot CI^3 - 2.63 \cdot CI^2 - 0.58 \cdot CI + 1$	Perez et al. (2002)
3	GHI = GHIcs · CSI CSI = 1.2, CI ≤ −0.2; CSI = 1.0 − CI, −0.2 < CI ≤ 0.8; CSI = $2.0667 - 3.6667 \cdot CI + 1.6667 \cdot CI^2$, 0.8 < CI ≤ 1.1; CSI = 0.05, 1.1 < CI.	Hammer et al. (2003)
4	GHI = GHIcs · CSI CSI = 1.2, CI ≤ −0.2; CSI = 1.0 − CI, −0.2 < CI ≤ 0.8; CSI = $1.1661 - 1.781 \cdot CI + 0.73 \cdot CI^2$, 0.8 < CI ≤ 1.05; CSI = 0.09, 1.05 < CI.	Mueller et al. (2012)

Table 5

Input parameters for the used clear-sky models. The variables are the solar constant I_0 [W m^{-2}], solar zenith angle θ [°], altitude h [m], Linke turbidity T_L, surface albedo ρ_g, local pressure P_a [mb], ambient temperature T_a [K], AOD at 550 nm τ_{550}, Ångström exponent α, total ozone amount u_{O_3} [atm-cm], total precipitable water vapor u_{H_2O} [cm], total nitrogen dioxide amount u_{NO_2} [atm-cm], relative humidity ϕ [%], wind speed V [m s^{-1}].

Clear-sky model	Input parameters	Data source	Reference
Ineichen–Perez	I_0, θ, h, T_L	SoDa database (Remund et al., 2003)	Perez et al. (2002)
McClear	I_0, θ, h, ρ_g, P_a, T_a, τ_{550}, α, u_{O_3}, u_{H_2O}	CAMS (Schroedter-Homscheidt et al., 2021)	Lefèvre et al. (2013)
REST2	I_0, θ, ρ_g, P_a, τ_{550}, α, u_{O_3}, u_{NO_2}, u_{H_2O}	NSRDB (Sengupta et al., 2018)	Gueymard (2008)
Ineichen–Perez TL[a]	I_0, θ, h, P_a, T_a, ϕ, V	Local measurements	Chen and Li (2022)

[a]Ineichen–Perez TL model is also based on T_L. Instead of using the SoDa database, the T_L is estimated from local meteorological measurements (P_a, T_a, ϕ, V) (Chen and Li, 2022).

more than one third clear-sky instants detected of the daytime are included (e.g., if the daytime of a day is 8 h, only when the detected clear-sky instants are more than 2.4 h, the day will be included in the dataset). It is also necessary to mention that the turbidity typically varies between 1 and 10 (Antonanzas-Torres et al., 2019), so any derived turbidity with the value less than 1 (or extremely high) should be excluded. The turbidity estimation model for each station is trained and validated separately. However, it is possible to build a more universal model by involving more locations using the same methodology. The estimated turbidity is then used as the input to calculate the GHIcs using PVLIB.

Since semi-empirical model (e.g., Heliosat −2 method) can be adapted to geostationary satellite in the visible band (0.4–1.1 μm) (Lefèvre et al., 2004), the GOES-16 blue band (visible, 0.47 μm), red band (visible, 0.64 μm), and veggie band (near-infrared, 0.87 μm) are applied and compared for 5 min GHI estimation in this work. Apart from different strategies described in Table 3 for determining CI, there are also different methods proposed to calculate the GHI (see Table 4). The detailed comparisons of the reported strategies, the proposed methods, as well as the applied clear-sky models for GHI estimation are presented in the following section. The performance evaluation metrics are RMSE, mean bias error (MBE), and their normalized counterparts nRMSE and nMBE defined by the following equations:

$$\text{RMSE} = \sqrt{\frac{1}{N} \sum (e_i - o_i)^2}$$

$$\text{nRMSE} = \frac{\sqrt{\frac{1}{N} \sum (e_i - o_i)^2}}{\frac{1}{N} \sum o_i}$$

$$\text{MBE} = \frac{1}{N} \sum (e_i - o_i)$$

$$\text{nMBE} = \frac{\sum (e_i - o_i)}{\sum o_i}$$

where e_i and o_i are the pair of GHI estimation and ground observation, N is the total number of compared data points.

3. Results and discussion

Despite difficulties associated in acquiring the input parameters, the REST2 model has been proved as the one of the best clear-sky models for estimating clear-sky irradiance (Sun et al., 2019). Given that the clear-sky irradiance of REST2 is available in the dataset of NSRDB and the fact that a better clear-sky model (i.e., McClear) can lead to better GHI estimation results (Qu et al., 2014), we use the REST2 GHIcs in the comparison of the GHI estimation performance based on different ABI bands, empirical regressions between CSI and CI, and methods to determine the CI. The information of used ABI bands is presented in Table 1, Table 3 details the strategies used for deriving CI, and the methods for GHI calculation via GHIcs, CSI, and CI are listed in Table 4. The comparison of different clear-sky models used in GHI estimation with semi-empirical method is then based on the combined approach (i.e., the ABI band, CI derivation, and GHI calculation) that is likely to obtain superior GHI estimation results.

3.1. Comparison of ABI bands and derivation methods for CI and CSI

Since the GOES-16 ABI bands have different spatial resolution, Band 2 (red) is re-scaled to the same resolution as Band 1 and Band 3. The comparison of upper and lower bounds determination based on different ABI bands and strategies at DRA is presented in Fig. 2. The upper bound from Band 1 has higher values than Bands 2 and 3, while Band 3 results in relatively lower upper bounds no matter what strategy is applied. Similarly, lower bound based on Band 1 turns to be higher, followed by Band 2 and Band 3 has the comparatively lower value. Unlike upper bounds that do not show many fluctuations, lower bounds have relatively larger variations. Compared with Strategies 1 and 2, Strategies 3 and 4 generally leads to larger upper bound and smaller
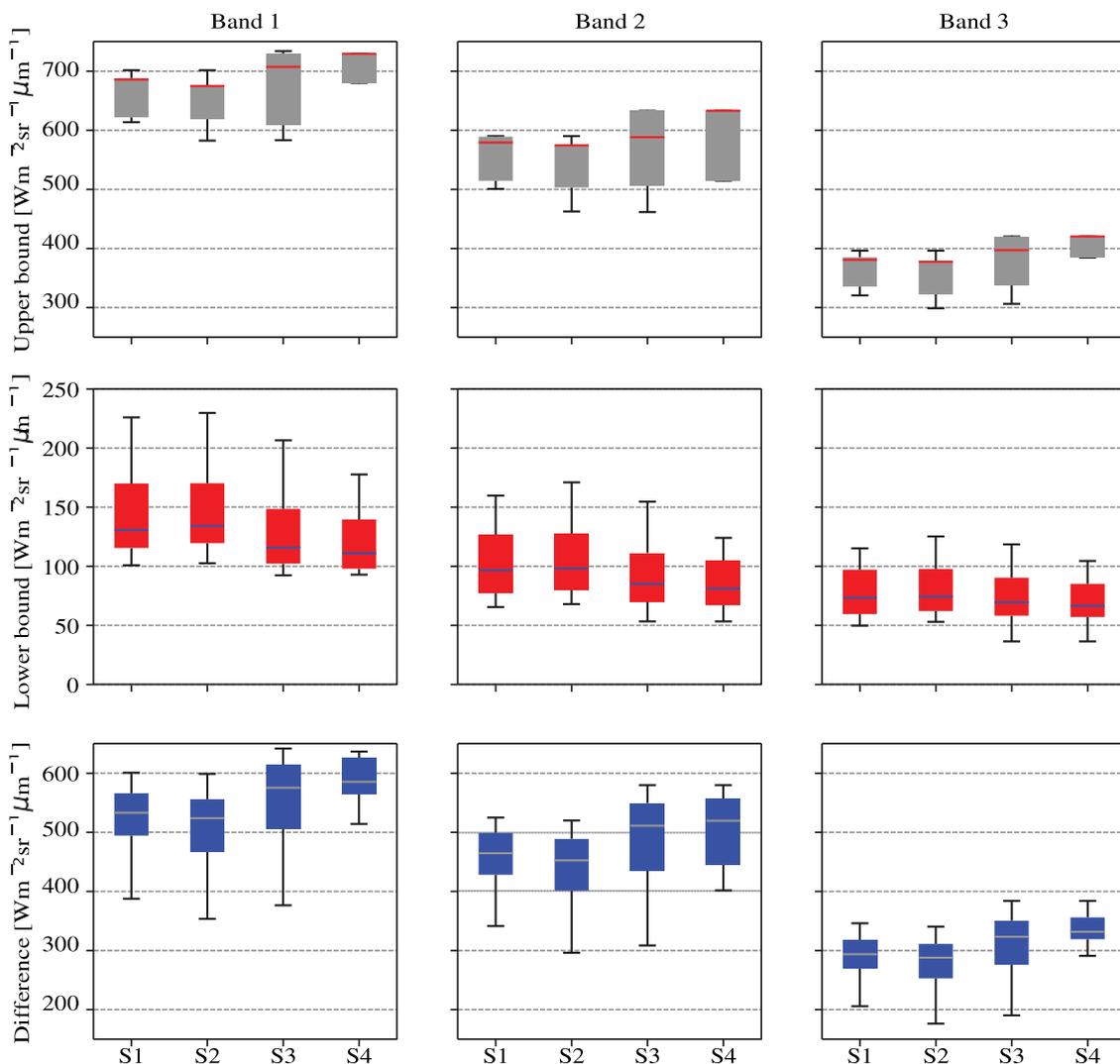
Fig. 2. Comparison of the upper bound and lower bound determination using different ABI bands (see Table 1) and strategies at DRA (2019-01-01 to 2019-05-31). S1–S4 are the symbols of strategies presented in Table 3. The differences between upper and lower bounds are also included for comparison.

lower bound. The reason could be the shorter periods and less points used for determining upper and lower bounds as shown in Table 3. This also results in wider dynamic ranges, i.e., the differences between upper and lower bounds, which exhibit similar trends with the upper bound, Band 1 leads to higher value than Bands 2 and 3, while Band 3 has the lowest value.

Upper and lower bounds are used to determine CI, CSI is then calculated from CI using empirical regressions (see Table 4). Fig. 3 shows the comparison of CSI calculations from different bands, CI derivation strategies, and CI-to-CSI methods, where the CSI reference is the ratio between GHI measurement and GHIcs from REST2 clear-sky model. Generally, the CSI derived from Band 1 has smaller divergences in terms of nRMSE and nMBE with the referenced CSI compared with the other two bands, while Band 3 shows relatively larger differences no matter what CI derivation strategy and CI-to-CSI method are applied. Among the used CI derivation strategies, they have comparable results in terms of nRMSE, while Strategies 3 and 4 produce lower biases compared with Strategies 1 and 2. Similarly, there is no huge difference when comparing the CI-to-CSI methods regarding nRMSE. However, Methods 3 and 4 are more likely to yield lower nMBE values. It is worthwhile to mention that the combination of Band 1, Strategy 4, and Method 3 (or Method 4) outperforms other combinations with comparatively smaller nRMSE and nMBE.

A detailed comparison of different bands and methods used to estimate GHI is illustrated in Fig. 4. Using Method 2 generally yields

GHI estimation with larger nRMSE and nMBE values, while the rest three methods have comparable GHI estimation results with similar nRMSE. Method 1 leads to slightly higher nMBE values than Methods 3 and 4. When it comes to the dynamic range and CI determination, all the strategies generate GHI estimation with nRMSE greater than 20% no matter which method is used, while Strategies 1 and 2 have slightly lager values. Moreover, Strategies 1 and 2 comparatively show larger discrepancies in nMBE than Strategies 3 and 4, while Strategy 4 produces the lowest nMBE. There is no significant difference (i.e., nRMSE and nMBE) in Methods 3 and 4 to calculate GHI via the relationship between CSI and CI regardless of which strategy is applied to derive the dynamic range and CI. The combination of Strategy 4 and Method 3 (or Method 4) is likely to generate GHI estimations with lower nRMSE and nMBE. Strategies 1 and 2 are proposed for GHI estimation at a rough time resolution (e.g., hourly), which might be inappropriate when the time resolution is much improved to 5 min. Therefore, the subsequent results and discussion are based on the combination of Strategy 4 and Method 3 in 5 min GHI estimation.

It is shown in Fig. 4 that Band 1 generally produces lower nRMSE and nMBE values than Bands 2 and 3 no matter which combination of method and strategy is applied in estimating GHI. The possible explanation could be that Band 1 results in higher upper and lower bounds as well as wider dynamic ranges (see Fig. 2), which are less sensitive to the uncertainties in sensor's measurements when determining the
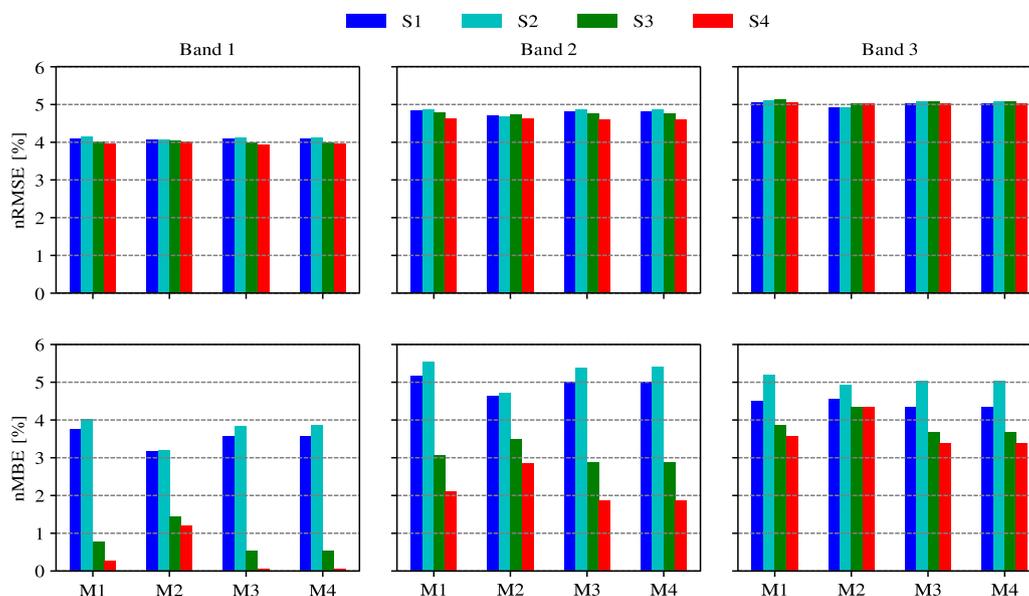
Fig. 3. The nRMSE and nMBE of the CSI reference and estimation based on different bands, dynamic range and CI derivation, and empirical regressions between CSI and CI at DRA (2019-01-01 to 2019-05-31). The reference CSI is determined using GHI measurements and REST2 clear-sky model. S1–S4 are the symbols of strategies presented in Table 3, and M1–M4 represent the empirical methods described in Table 4.
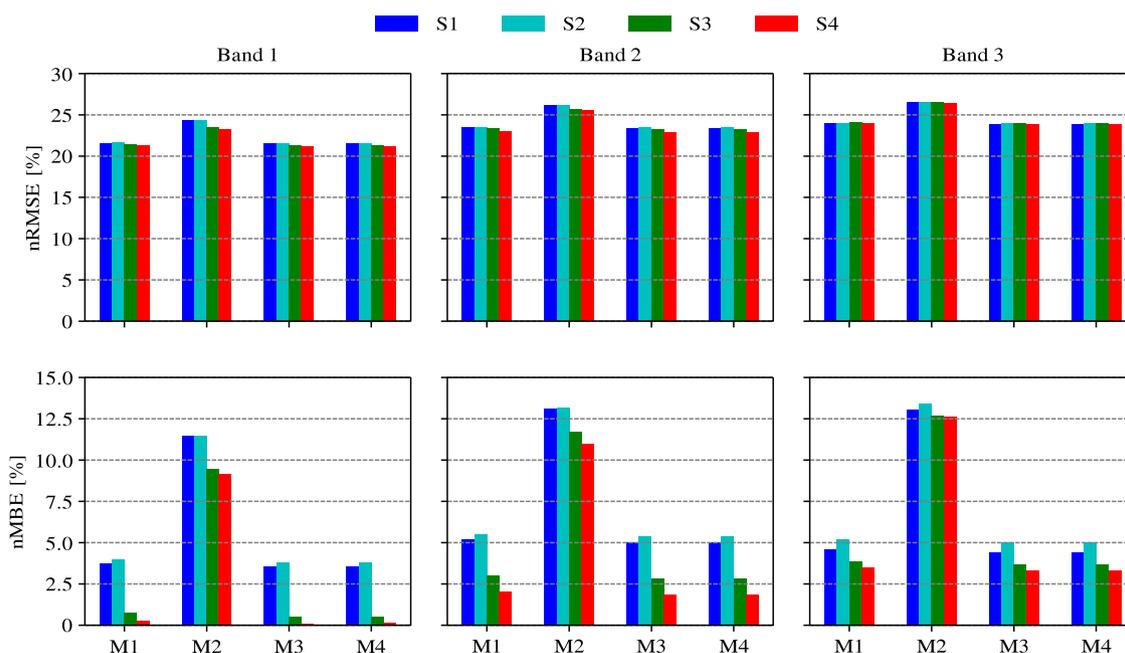

Fig. 4. The nRMSE and nMBE between the GHI measurements and estimations based on different bands, dynamic range and CI derivation, and empirical regressions between GHI and CI using REST2 clear-sky model at DRA (2019-01-01 to 2019-05-31). S1–S4 are the symbols of strategies presented in Table 3, and M1–M4 represent the empirical methods described in Table 4.

dynamic range for CI derivation. Therefore, the estimated CSI from Band 1 show comparatively lower discrepancies than Bands 2 and 3 (see Fig. 3) and thus better GHI estimations. To further evaluate the performance of GHI estimation using different ABI bands, it is necessary to ensure that the used methods, data points, and time periods are the same. Therefore, the REST2 clear-sky model, Strategy 4, and Method 3 are set as the preconditions for comparing the ABI bands used in semi-empirical model for GHI estimation.

Table 6 details the performance of different ABI bands used for GHI estimation. Band 1 generates the lowest divergence with a nRMSE of 21.47% and a nMBE of 1.41%, while Band 3 produces the largest nRMSE of 24.35% and nMBE of 4.46%. The reflective spectral radiance measured by the ABI sensor used in GHI estimation with semi-empirical

models leads to decreased performance when using bands with larger wavelength. It is worthwhile to mention that the GHI estimates based on Band 1 using semi-empirical model have slightly lower errors of nRMSE and nMBE than the results from NSRDB, which means the semi-empirical model may produce comparable results with physical models but with less complexity.

3.2. Comparison of clear-sky models for GHI estimation

Based on the results from the previous subsections, a better GHI estimation is achieved using the measurements of ABI Band 1, the Strategy 4 for dynamic range and CI determination, and the Method 3 for CI to GHI conversion. At this stage, the prerequisites for evaluating

Table 6
Summary of the ABI band performance in 5 min GHI estimation using RSET2 clear-sky model, Strategy 4, and Method 3 at DRA (2019-01-01 to 2019-05-31). The GHI estimation from NSRDB is also included as reference.

Band	RMSE [W m^{-2}]	nRMSE [%]	MBE [W m^{-2}]	nMBE [%]
1	109.37	21.47	7.18	1.41
2	117.73	23.11	15.21	2.99
3	124.05	24.35	22.75	4.46
NSRDB	110.79	21.74	−13.44	−2.64

Table 7
The overall nRMSE [%] and nMBE [%] between GHI estimations and measurements at seven SURFRAD stations using semi-empirical method with different clear-sky models under four evaluation cases (all-sky, cloudy days, partially cloudy days, and clear days). The GHI estimation from NSRDB is also included for comparison.

	All-sky[a]		Cloudy days[b]		Partially cloudy days[c]		Clear days[d]	
	nRMSE	nMBE	nRMSE	nMBE	nRMSE	nMBE	nRMSE	nMBE
Ineichen–Perez	25.43	2.03	37.60	9.20	19.54	−1.61	5.77	−4.62
McClear	25.38	5.42	38.03	11.87	19.23	1.94	2.55	0.62
REST2	25.19	4.87	37.68	11.32	19.13	1.45	2.53	−0.15
Ineichen–Perez TL	25.53	5.22	38.36	12.80	19.24	1.23	2.53	−1.11
NSRDB	25.25	−0.45	38.37	−1.50	18.75	0.23	2.37	0.45

[a]'All-sky' means the whole time period with cloudy, partially cloudy and clear days.
[b]'Cloudy days' means the days without clear-sky periods or the detected clear-sky instants are less than one third of the daytime.
[c]'Partially cloudy days' includes the days with cloudless periods (more than one third of the daytime).
[d]'Clear days' only involves the cloudless days.

the performance of different clear-sky models in GHI estimation using semi-empirical model have been settled. The following sections present the comparisons between different clear-sky models applied in semi-empirical method under different sky conditions. We use two types of methods for classifying sky conditions here: one is based on days, in which the days are classified as cloudy, partially cloudy, and clear days (Scolari et al., 2018); The other one is based on periods, where the instants are grouped as cloudy and clear periods (Larson et al., 2020). In specific, clear and cloudy instants are detected using the Bright-Sun method with ground irradiance measurements (Bright et al., 2020) and then clustered as clear/cloudy/partially cloudy days and clear/cloudy periods.

3.2.1. Comparison under cloudy, partially cloudy and clear days

The overall performance of GHI estimation using semi-empirical method with different clear-sky models is shown in Table 7. There is no significant discrepancy between clear-sky models in GHI estimation under conditions of all-sky, cloudy, and partially cloudy. REST2 is likely to generate slightly lower nRMSE in all-sky and partially cloudy conditions, while Ineichen–Perez yields the lowest nRMSE when only cloudy days are considered. Compared with the physical model based GHI estimation results in NSRDB, using semi-empirical model produces GHI estimates with similar or slightly larger nRMSE no matter which clear-sky model is applied. However, there are comparatively larger biases (i.e., nMBE) in semi-empirical methods under most conditions. Semi-empirical methods are more possibly to have overestimated results, especially in the cloudy days. Although Ineichen–Perez produces the lowest nMBE in all-sky and cloudy conditions, it does not mean Ineichen–Perez provides better clear-sky irradiance estimations. The low overall bias of Ineichen–Perez in GHI estimations is a compromise of the overestimation in semi-empirical methods and the underestimation in Ineichen–Perez's clear-sky irradiance, since the Ineichen–Perez based GHI estimations in partially cloudy and clear-sky days show negative biases of −1.61% and −4.62%, respectively.

The primary uncertainty for GHI estimation is caused by the clouds for both physical and semi-empirical methods. The nRMSE of GHI estimates in cloudy days are in the range of 37.60%–38.37%, which is approximate two times of the nRMSE in partially cloudy days (18.75%–19.54%). The nRMSE in clear-sky days are around 2.50% besides Ineichen–Perez, which has a larger value of 5.77%. Since clouds are the primary factor affecting the solar irradiance reaching the ground level,

it is necessary to improve the method to account the irradiance attenuation caused by clouds for both physical and semi-empirical models. That said, the future research on satellite-based solar resourcing could be the improvements of satellite-derived cloud properties (for physical model) and cloud attenuation determinations (for semi-empirical model).

Fig. 5 presents the detailed comparison of different clear-sky models for GHI estimation using semi-empirical method at seven SURFRAD stations under four sky conditions. The GHI estimations based on four clear-sky models have comparable results in terms of nRMSE under all-sky, cloudy and partially cloudy conditions, while Ineichen–Perez tends to generate larger nRMSE values in clear-sky days. Compared with the physical model based GHI estimation results in NSRDB, using semi-empirical model produces GHI estimates with similar or slightly lower nRMSE at most SURFRAD stations except TBL, where the occurrence of cloudy days is comparatively higher. For each individual station, the GHI estimation under cloudy days is most likely associated with the largest uncertainties of nRMSE and nMBE. The lower biases of Ineichen–Perez based GHI estimations under all-sky and cloudy conditions are shown in some of the stations (i.e., BON, GWN, PSU, and SXF), whose biases are apparently higher in partially cloudy and clear conditions compared with other clear-sky models, proving the overestimation in semi-empirical methods and the underestimation in Ineichen–Perez's clear-sky irradiance.

3.2.2. Comparison under cloudy and clear periods

To further evaluate the performance of GHI estimation using semi-empirical model under different conditions, the sky is divided into cloudy and clear based on periods. The overall comparison at seven SURFRAD stations is shown in Table 8. Similarly, the GHI estimation in cloudy periods is associated with larger uncertainties (e.g., nRMSE), and semi-empirical model is likely to yield higher bias than the physical model. In cloudless periods, all the clear-sky models except Ineichen–Perez produce comparable results with NSRDB. When using GHIcs directly as the GHI estimates, Ineichen–Perez generates the largest errors, and Ineichen–Perez TL yields better results than other three clear-sky models.

The detailed comparison of GHI estimation under cloudy and clear instants for all the SURFRAD stations is presented in Fig. 6. Semi-empirical model tends to overestimate GHI with comparatively larger positive biases in cloudy periods, and the highest bias can be about 15%
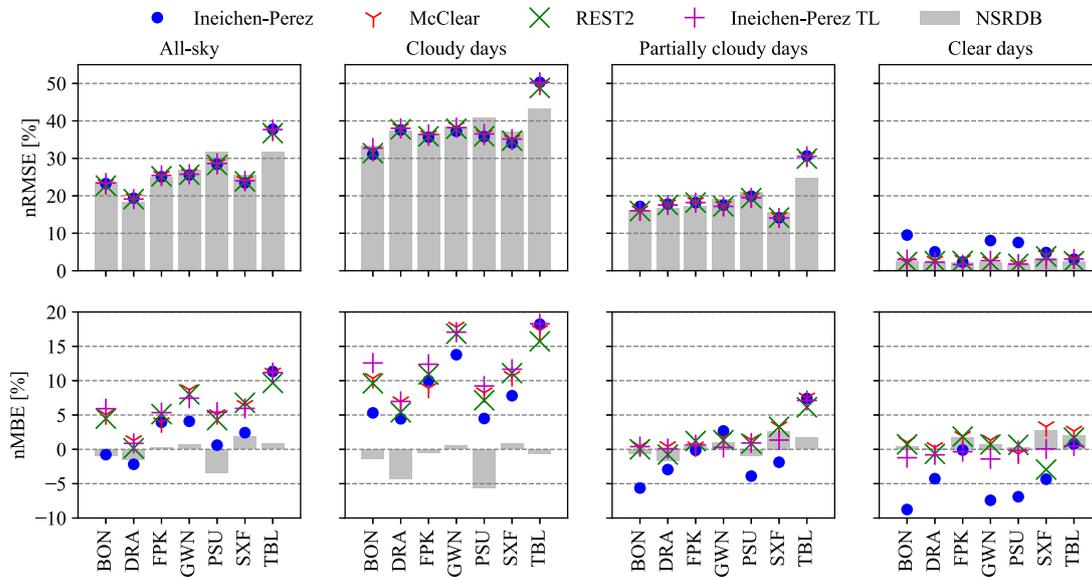
Fig. 5. The nRMSE and nMBE between the measured and estimated GHI for four clear-sky models in semi-empirical method, seven SURFRAD stations, and four evaluated conditions (all-sky, cloudy days, partially cloudy days, and clear days). GHI estimation from NSRDB is also included for comparison.

Table 8
The overall nRMSE [%] and nMBE [%] between GHI estimations and measurements at seven SURFRAD stations using semi-empirical method with different clear-sky models under three evaluation cases (all-sky, cloudy periods, and clear periods). The GHI estimation from NSRDB is also included.

	All-sky[a]		Cloudy periods[b]		Clear periods[c]		GHIcs[d]	
	nRMSE	nMBE	nRMSE	nMBE	nRMSE	nMBE	nRMSE	nMBE
Ineichen–Perez	25.43	2.03	31.23	5.03	5.37	−3.93	4.86	−3.29
McClear	25.38	5.42	31.36	8.87	2.98	0.56	2.54	1.22
REST2	25.19	4.87	31.12	8.23	2.91	−0.07	2.43	0.52
Ineichen–Perez TL	25.53	5.22	31.54	9.20	2.81	−0.86	2.16	−0.20
NSRDB	25.25	−0.45	31.21	−1.01	2.43	0.52	–	–

[a] 'All-sky' means the whole time period with cloudy and clear instants.
[b] 'Cloudy periods' contains the periods are detected as cloudy.
[c] 'Clear periods' includes all the detected cloudless periods.
[d] 'GHIcs' is to use GHIcs directly as GHI estimation in clear periods.

at TBL. In the application of semi-empirical method, Ineichen–Perez generally produces lower bias than the other three clear-sky models under cloudy conditions. However, in cloudless periods, Ineichen–Perez is likely to produce GHI estimation with larger discrepancies. The possible explanation for this is the same as the phenomenon that Ineichen–Perez produces GHI estimation with lower biases in all-sky and cloudy days as discussed in Section 3.2.1.

3.2.3. Comparison between physical and semi-empirical methods for GHI estimation

In physical model for GHI estimation, the GHIcs is directly used as the GHI estimate when the sky is free from cloud. Where the accuracy of used clear-sky model is crucial for the overall GHI estimation performance. Generally, physical GHI estimation methods apply physical clear-sky models, for instance, REST2 in NSRDB, McClear in Heliosat −4. It might be of interest to compare the performance of GHI estimation using semi-empirical and physical models under clear-sky conditions. As shown in Table 8, it is more likely to generate GHI results with relatively lower nRMSE values using GHIcs as GHI estimates (nRMSE ranges from 2.16% to 4.86%) than CI based method (nRMSE varies from 2.81%–5.37%). The situation of nMBE differs, McClear and REST2 produce larger biases, while Ineichen–Perez and Ineichen–Perez TL yield slightly lower nMBE values. It is worthwhile to mention that Ineichen–Perez TL has the lowest nRMSE and nMBE, which means Ineichen–Perez TL has the potential to improve GHI estimation in physical models.

The detailed comparison of GHI estimates using semi-empirical model and GHIcs for SURFRAD stations is presented in Fig. 7. Generally, both estimated and GHIcs of Ineichen–Perez show larger nRMSE and nMEB at most of the stations except FPK. Better clear-sky models, such as McClear and REST2, are likely to produce better GHI estimations with relatively lower nRMSE and nMBE in cloudless periods using both semi-empirical and physical models. Ineichen–Perez tends to yield negative biases in GHI estimations or using GHIcs directly due to its underestimation of clear-sky irradiance. Ineichen–Perez TL produces comparable results with McClear and REST2 in terms of nRMSE, while the biases tend to be smaller. For McClear, REST2, and Ineichen–Perez TL, using the semi-empirical model is probably to generate GHI estimation with larger nRMSE and nMBE compared with the direct GHI estimates from GHIcs. Which means another challenge of semi-empirical method is how to improve the CI and CSI derivation considering the variations in clear-sky irradiance caused by the dynamics of aerosol and water vapor in the atmosphere.

All the applied clear-sky models yield comparable overall results of GHI estimations (see Tables 7 and 8) using semi-empirical method, REST2 has the lowest nRMSE of 25.19% while Ineichen–Perez TL has the highest nRMSE of 25.53%. Ineichen–Perez performs better than other clear-sky models in terms of nRMSE and nMBE under cloudy conditions, while Ineichen–Perez TL produces the largest nRMSE and nMBE. Although Ineichen–Perez has the lowest biases in GHI estimation under all-sky and cloudy conditions, it does not mean that Ineichen–Perez provides better clear-sky irradiance, as there is a compromise of
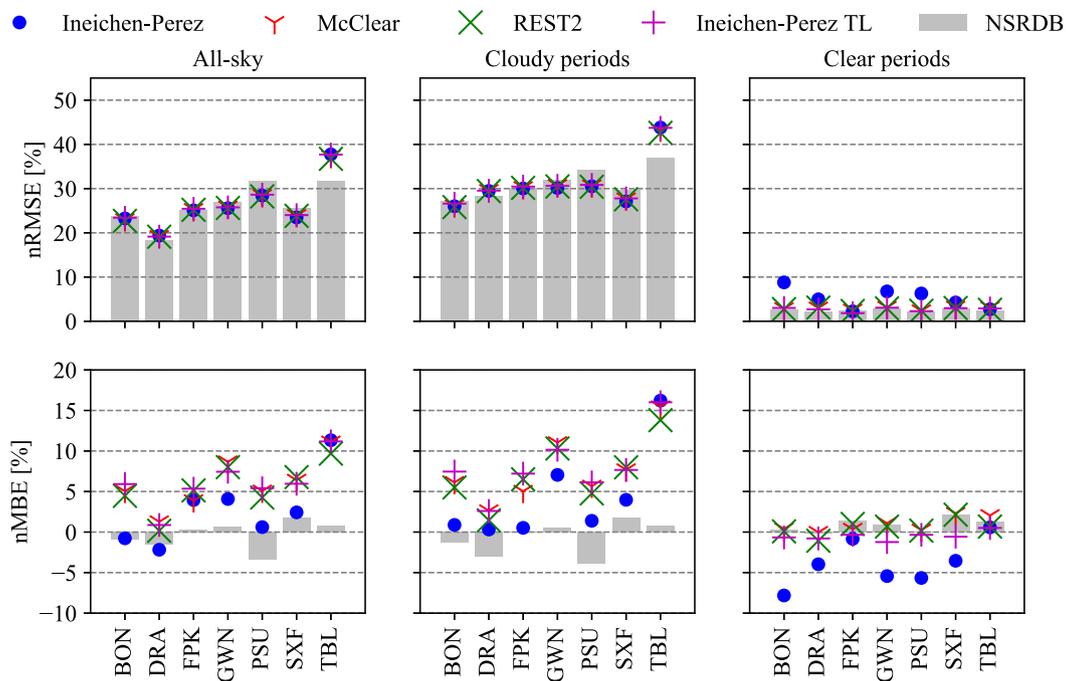
Fig. 6. The nRMSE and nMBE between the GHI measurements and estimates using semi-empirical method for four clear-sky models, seven SURFRAD stations, and three evaluation conditions (all-sky, cloudy periods, and clear periods).

the overestimation of GHI using semi-empirical model and the underestimation of Ineichen–Perez's GHIcs. Ineichen–Perez tends to generate negative biases in clear conditions, with the largest nMBE of −4.62% in clear-sky days and −3.93% in cloudless periods. When comparing the two physical clear-sky models of McClear and REST2 in the application of semi-empirical method, REST2 outperforms McClear in all the sky conditions with slightly lower nRMSE and nMBE. Compared with Ineichen–Perez, Ineichen–Perez TL has lower values of nRMSE and nMBE in partially cloudy days and clear conditions. The GHI estimation in each individual station (see Figs. 5 and 6) exhibits similar results as the overall picture but with some site-specific divergences. It is important to note that Ineichen–Perez TL generally performs better than other clear-sky models when using GHIcs as the GHI estimations in clear periods with comparatively lower nRMSE and nMBE.

4. Conclusions

In this work, different strategies for dynamic range and CI determination, methods to calculate GHI via GHIcs, CSI and CI are compared in 5 min averaged GHI estimation using semi-empirical model and GOES-16 images. Then, a comparison of three different ABI bands (i.e., blue, red, veggie) in GHI estimation is performed. Finally, the performance of four clear-sky models in GHI estimation using the same semi-empirical method is evaluated under different sky conditions. The key findings are:

- More accurate 5 min averaged GHI estimates are achieved using a fixed time window (i.e., Strategy 4), Method 3 (or Method 4) of GHI conversion from CI and CSI, and Band 1 for solar resourcing applications (e.g., GHI assessment). A fixed time window is easy to implement without much computing resource, but it is not suitable for operational applications, such as solar forecasting, where a moving time window is required.
- There is no significant difference in GHI estimation using different clear-sky models, the semi-empirical model yields comparable results compared with the NSRDB, but with comparatively larger biases. Semi-empirical model tends to overestimate the GHI in

cloudy conditions, the uncertainties in cloudy periods are noticeably higher than cloud free conditions. Therefore, it is crucial to determine the irradiance attenuation caused by clouds for both physical and semi-empirical models.

- In the application of semi-empirical method, Ineichen–Perez has lower biases under all-sky and cloudy conditions, this does not mean Ineichen–Perez provides better clear-sky irradiance due to the compromise of overestimation in semi-empirical model and Ineichen–Perez's underestimation of clear-sky irradiance. REST2 generally outperforms McClear under all sky conditions.
- Ineichen–Perez TL, as a modified model based on estimated turbidity, provides GHI estimation using semi-empirical method with slightly larger values of nRMSE and nMBE in all-sky and cloudy conditions. The performance of Ineichen–Perez TL under partially cloudy day and clear periods is comparable with McClear and REST2, and comparatively better than Ineichen–Perez. When using clear-sky irradiance as the direct estimation of GHI, Ineichen–Perez TL has a better performance.
- A better clear-sky model (e.g., REST2 versus McClear) can generally lead to better GHI estimation using semi-empirical method. Considering the difficulties associated in obtaining the atmospheric inputs of REST2, and the limited divergences in GHI estimation between these two clear-sky models, McClear is more appropriate due to its global availability. Ineichen–Perez TL provides better clear-sky irradiance for clear-sky conditions, therefore has the potential for the improvements in physical models where clear-sky irradiance is directly used as GHI estimation.

Declaration of competing interest

The authors declare that they have no known competing financial interests or personal relationships that could have appeared to influence the work reported in this paper.
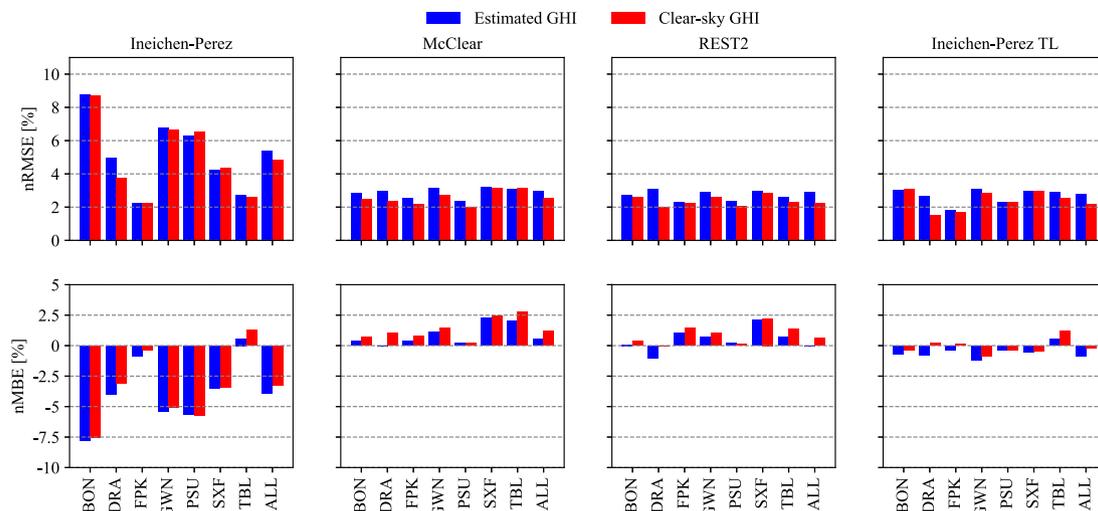
Acknowledgments

Fig. 7. The nRMSE and nMBE between the GHI measurements and estimates in clear periods for four clear-sky models, and seven SURFRAD stations. 'ALL' means all the seven stations are included. 'Estimated GHI' means the GHI estimates of semi-empirical model. 'Clear-sky GHI' means the GHIcs directly calculated from clear-sky models.

References

Goes R series product definition and users' guide (PUG) volume 3: Level 1B products. Available at: https://www.goes-r.gov/users/docs/PUG-L1b-vol3.pdf.

Albarelo, T., Marie-Joseph, I., Primerose, A., Seyler, F., Wald, L., Linguet, L., 2015. Optimizing the Heliosat-II method for surface solar irradiation estimation with GOES images. Can. J. Remote Sens. 41 (2), 86–100.

Antonanzas-Torres, F., Urraca, R., Polo, J., Perpiñán Lamigueiro, O., Escobar, R., 2019. Clear sky solar irradiance models: A review of seventy models. Renew. Sustain. Energy Rev. 107, 374–387.

Arbizu-Barrena, C., Ruiz-Arias, J.A., Rodríguez-Benítez, F.J., Pozo-Vázquez, D., Tovar-Pescador, J., 2017. Short-term solar radiation forecasting by advecting and diffusing MSG cloud index. Sol. Energy 155, 1092–1103.

Augustine, J.A., DeLuisi, J.J., Long, C.N., 2000. SURFRAD–A national surface radiation budget network for atmospheric research. Bull. Am. Meteorol. Soc. 81 (10), 2341–2358.

Ayompe, L.M., Duffy, A., 2014. An assessment of the energy generation potential of photovoltaic systems in Cameroon using satellite-derived solar radiation datasets. Sustain. Energy Technol. Assess. 7, 257–264.

Beyer, H.G., Costanzo, C., Heinemann, D., 1996. Modifications of the Heliosat procedure for irradiance estimates from satellite images. Sol. Energy 56 (3), 207–212.

Bright, J.M., Sun, X., Gueymard, C.A., Acord, B., Wang, P., Engerer, N.A., 2020. Bright-Sun: A globally applicable 1-min irradiance clear-sky detection model. Renew. Sustain. Energy Rev. 121, 109706.

Broxton, P., Zeng, X., Dawson, N., 2019. Daily 4 km Gridded SWE and Snow Depth from Assimilated In-Situ and Modeled Data Over the Conterminous US, Version 1. NASA National Snow and Ice Data Center Distributed Active Archive Center, Boulder, CO.

Cano, D., Monget, J.-M., Albuisson, M., Guillard, H., Regas, N., Wald, L., 1986. A method for the determination of the global solar radiation from meteorological satellite data. Sol. Energy 37 (1), 31–39.

Chen, S., Li, M., 2022. Improved turbidity estimation from local meteorological data for solar resourcing and forecasting applications. Renew. Energy 189, 259–272.

Chu, Y., Li, M., Coimbra, C.F.M., 2016. Sun-tracking imaging system for intra-hour DNI forecasts. Renew. Energy 96, 792–799.

Chu, Y., Li, M., Coimbra, C.F.M., Feng, D., Wang, H., 2021. Intra-hour irradiance forecasting techniques for solar power integration: A review. iScience 103136.

Chu, Y., Pedro, H.T.C., Coimbra, C.F.M., 2013. Hybrid intra-hour DNI forecasts with sky image processing enhanced by stochastic learning. Sol. Energy 98, 592–603.

Garniwa, P., A. A. Ramadhan, R., Lee, H.-J., 2021. Application of semi-empirical models based on satellite images for estimating solar irradiance in Korea. Appl. Sci. 11 (8), 3445.

Gueymard, C.A., 2008. REST2: High-performance solar radiation model for cloudless-sky irradiance, illuminance, and photosynthetically active radiation–validation with a benchmark dataset. Sol. Energy 82 (3), 272–285.

Hammer, A., Heinemann, D., Hoyer, C., Kuhlemann, R., Lorenz, E., Müller, R., Beyer, H.G., 2003. Solar energy assessment using remote sensing technologies. Remote Sens. Environ. 86 (3), 423–432.

Harty, T.M., Holmgren, W.F., Lorenzo, A.T., Morzfeld, M., 2019. Intra-hour cloud index forecasting with data assimilation. Sol. Energy 185, 270–282.

Holmgren, W.F., Hansen, C.W., Mikofski, M.A., 2018. Pvlib python: A python package for modeling solar energy systems. J. Open Source Softw. 3 (29), 884.

IEA, 2020. Solar PV. [online], Available at: https://www.iea.org/reports/solar-pv. (Accessed 4 October 2021).

Ineichen, P., Perez, R., 2002. A new airmass independent formulation for the Linke turbidity coefficient. Sol. Energy 73 (3), 151–157.

Inman, R.H., Pedro, H.T.C., Coimbra, C.F.M., 2013. Solar forecasting methods for renewable energy integration. Prog. Energy Combust. Sci. 39 (6), 535–576.

Jia, D., Hua, J., Wang, L., Guo, Y., Guo, H., Wu, P., Liu, M., Yang, L., 2021. Estimations of global horizontal irradiance and direct normal irradiance by using Fengyun-4A satellite data in Northern China. Remote Sens. 13 (4), 790.

Kallio-Myers, V., Riihelä, A., Lahtinen, P., Lindfors, A., 2020. Global horizontal irradiance forecast for Finland based on geostationary weather satellite data. Sol. Energy 198, 68–80.

Kleissl, J., 2013. Solar Energy Forecasting and Resource Assessment. Academic Press.

Laguarda, A., Giacosa, G., Alonso-Suárez, R., Abal, G., 2020. Performance of the site-adapted CAMS database and locally adjusted cloud index models for estimating global solar horizontal irradiation over the Pampa Húmeda. Sol. Energy 199, 295–307.

Larson, D.P., Li, M., Coimbra, C.F.M., 2020. SCOPE: Spectral cloud optical property estimation using real-time GOES-R longwave imagery. J. Renew. Sustain. Energy 12 (2), 026501.

Lefèvre, M., Albuisson, M., Wald, L., 2004. Description of the software Heliosat-2 for the conversion of images acquired by Meteosat satellites in the visible band into maps of solar radiation available at ground level.

Lefèvre, M., Oumbe, A., Blanc, P., Espinar, B., Gschwind, B., Qu, Z., Wald, L., Schroedter-Homscheidt, M., Hoyer-Klick, C., Arola, A., et al., 2013. McClear: A new model estimating downwelling solar radiation at ground level in clear-sky conditions. Atmos. Meas. Tech. 6 (9), 2403–2418.

Li, M., Chu, Y., Pedro, H.T.C., Coimbra, C.F.M., 2016. Quantitative evaluation of the impact of cloud transmittance and cloud velocity on the accuracy of short-term DNI forecasts. Renew. Energy 86, 1362–1371.

Lorenzo, A.T., Morzfeld, M., Holmgren, W.F., Cronin, A.D., 2017. Optimal interpolation of satellite and ground data for irradiance nowcasting at city scales. Sol. Energy 144, 466–474.

Mayer, B., Kylling, A., 2005. The libRadtran software package for radiative transfer calculations-description and examples of use. Atmos. Chem. Phys. 5 (7), 1855–1877.

Mouhamet, D., Tommy, A., Primerose, A., Laurent, L., 2018. Improving the Heliosat-2 method for surface solar irradiation estimation under cloudy sky areas. Sol. Energy 169, 565–576.

Mueller, R., Behrendt, T., Hammer, A., Kemper, A., 2012. A new algorithm for the satellite-based retrieval of solar surface irradiance in spectral bands. Remote Sens. 4 (3), 622–647.

Mueller, R.W., Dagestad, K.-F., Ineichen, P., Schroedter-Homscheidt, M., Cros, S., Dumortier, D., Kuhlemann, R., Olseth, J.A., Piernavieja, G., Reise, C., Wald, L., Heinemann, D., 2004. Rethinking satellite-based solar irradiance modelling: The SOLIS clear-sky module. Remote Sens. Environ. 91 (2), 160–174.

Murphy, P., 2021. 2020 Annual Report. Report, IEA Solar Heating & Cooling Programme.

Perez, R., Ineichen, P., Moore, K., Kmiecik, M., Chain, C., George, R., Vignola, F., 2002. A new operational model for satellite-derived irradiances: Description and validation. Sol. Energy 73 (5), 307–317.

Qu, Z., Gschwind, B., Lefèvre, M., Wald, L., 2014. Improving HelioClim-3 estimates of surface solar irradiance using the McClear clear-sky model and recent advances in atmosphere composition. Atmos. Meas. Tech. 7 (11), 3927–3933.

Qu, Z., Oumbe, A., Blanc, P., Espinar, B., Gesell, G., Gschwind, B., Klüser, L., Lefèvre, M., Saboret, L., Schroedter-Homscheidt, M., 2017. Fast radiative transfer parameterisation for assessing the surface solar irradiance: The Heliosat-4 method. Meteorol. Z. 26 (1), 33–57.

Remund, J., Wald, L., Lefèvre, M., Ranchin, T., Page, J., 2003. Worldwide Linke turbidity information. In: ISES Solar World Congress 2003, vol. 400. International Solar Energy Society (ISES), pp. 13–13.

Rigollier, C., Bauer, O., Wald, L., 2000. On the clear sky model of the ESRA—European solar radiation Atlas—with respect to the Heliosat method. Sol. Energy 68 (1), 33–48.

Rigollier, C., Lefèvre, M., Wald, L., 2004. The method Heliosat-2 for deriving shortwave solar radiation from satellite images. Sol. Energy 77 (2), 159–169.

Rigollier, C., Wald, L., 1999a. The HelioClim project: From satellite images to solar radiation maps. In: Proceedings of the ISES Solar World Congress. Citeseer.

Rigollier, C., Wald, L., 1999b. Selecting a clear-sky model to accurately map solar radiation from satellite images. In: EARSeL Symposium 1999 "Remote Sensing in the 21st Century: Economic and Environmental Applications". Balkema, pp. 131–137.

Schmit, T.J., Lindstrom, S.S., Gerth, J.J., Gunshor, M.M., 2018. Applications of the 16 spectral bands on the advanced baseline imager (ABI). J. Oper. Meteorol. 6 (4), 33–46.

Schroedter-Homscheidt, M., Azam, F., Betcke, J., Hoyer-Klick, C., Lefèvre, M., Wald, L., Wey, E., Saboret, L., 2021. User's Guide to the CAMS Radiation Service (CRS): Status December 2020. Copernicus Atmosphere Monitoring Service.

Scolari, E., Sossan, F., Haure-Touzé, M., Paolone, M., 2018. Local estimation of the global horizontal irradiance using an all-sky camera. Sol. Energy 173, 1225–1235.

Sengupta, M., Xie, Y., Lopez, A., Habte, A., Maclaurin, G., Shelby, J., 2018. The national solar radiation database (NSRDB). Renew. Sustain. Energy Rev. 89, 51–60.

Solcast, 2021. Inputs and algorithms. [online], Available at: https://solcast.com/historical-and-tmy/inputs-and-algorithms/. (Accessed 4 October 2021).

Sun, X., Bright, J.M., Gueymard, C.A., Acord, B., Wang, P., Engerer, N.A., 2019. Worldwide performance assessment of 75 global clear-sky irradiance models using principal component analysis. Renew. Sustain. Energy Rev. 111, 550–570.

Williamson, S., Businger, S., Matthews, D., 2018. Development of a solar irradiance dataset for Oahu, Hawai'i. Renew. Energy 128, 432–443.

Yagli, G.M., Yang, D., Gandhi, O., Srinivasan, D., 2020. Can we justify producing univariate machine-learning forecasts with satellite-derived solar irradiance? Appl. Energy 259, 114122.

Yang, D., 2020. Choice of clear-sky model in solar forecasting. J. Renew. Sustain. Energy 12 (2), 026101.

Yang, D., 2021. Validation of the 5-min irradiance from the national solar radiation database (NSRDB). J. Renew. Sustain. Energy 13 (1), 016101.

Zeng, X., Broxton, P., Dawson, N., 2018. Snowpack change from 1982 to 2016 over conterminous United States. Geophys. Res. Lett. 45 (23), 12–940.

Zhong, X., Kleissl, J., 2015. Clear sky irradiances using REST2 and MODIS. Sol. Energy 116, 144–164.